Soft Matter

COMMUNICATION

View Article Online
View Journal | View Issue

Cite this: *Soft Matter*, 2022, **18**, 6148

Received 21st June 2022,
Accepted 4th August 2022

DOI: 10.1039/d2sm00823h

rsc.li/soft-matter-journal

Helical micro-swimmer: hierarchical tail design and propulsive motility

Z. Y. Zhang,[ab] Y. F. Wang,[c] J. T. Kang,[d] X. H. Qiu[a] and C. G. Wang *[a]

Helical micro-swimmers have markedly extended the reach of human beings in numerous fields, ranging from *in vitro* tasks in lab-on-a-chip to *in vivo* applications for minimally invasive medicine. The previous studies on the propulsive motility optimization of the micro-swimmers mainly focused on the distinct actuation principles (*e.g.*, chemically powered, magnetic- or ultrasound energy-driven) and paid little attention to the structural design of these swimming machines themselves. The improvements of the structures can assist the externally powered motors in providing propulsion in a tiny scale and satisfy the agile locomotion demands. This paper presents the design, mechanics modeling and available experiments of a novel type of hierarchical helical swimming robot that significantly enhances the motility of the helix-based swimmers. Validated by the resistive force theory, our numerical model can well analyze the mechanical properties with a variety of geometric parameters. The motion performance of the hierarchical and conventional helical structures in low Reynolds regimes is presented, highlighting the advantages of hierarchical swimmers over the existing typical swimmers. In addition, the stability and resilience of the hierarchical swimmers can be maintained at a decent level. Moreover, the variable forward velocity resulting from the combined hierarchical structures is investigated here, which can thereby serve as a reliable design strategy. The proposed hierarchical helical design enables enticing opportunities for various device systems of medical robots and bio-integrated electronics.

Introduction

Helical structures have a widespread presence in a diversified range of areas, from macroscopic celestial motion to the double helix structure of deoxyribonucleic acid (DNA)[1] as the basis of life, to microscopic bacteria,[2,3] to the spiral growth of vines[4] and so on (see in Fig. 1). Recently, helix-based applications have received much more attention, such as artificial helical swimmers for targeted therapies or non-invasive surgical procedures,[5–7] mechanical assembly of the helix in reconfigurable systems for multifunctional electronics,[8] self-propelling actuators *via* light-driven helical structures,[9] helical bundles with high thermodynamic stability,[10] and helical mesostructures for three-dimensional flexible electronic devices.[11] In particular, the mechanical and functional performances of the helical micro-robots based on microscale hydrodynamics are attractive since they revolutionize the medical applications of robotic technologies toward improving human health care.[12]

The fundamental principles of helical swimming machines, with rich underlying physics and chemistry, have been discussed in several comprehensive articles.[13,14] A dimensionless experimental study on the geometrical parameters is proposed to investigate the influential geometrical parameters on the swimming performance of the helix.[15] Furthermore, coupling the structural and magnetic properties of artificial helical micro-swimmers with the dynamic properties of the flow field enables enticing opportunities for micro-robots to navigate inside obstructed, heterogeneous, and dynamically changing environments.[16] Acoustic, optical, and electrical energies can also be harvested to drive the motion of micro/nanostructures with unique principles.[13,17,18] In contrast to the remarkable diversity in helical architectures realized in experiments, analytical or semi-analytical solutions in relatively concise form only exist for a few simple geometries, such as a symmetrical helix with a certain radial radius. Seminal work demonstrates one efficient approach to understand the generation of the drag and thrust force by considering each segment of the helical tail as an independent slender rod.[19,20] The underlying assumption is that the hydrodynamic forces are proportional to the local body velocity, with the constant of proportionality being defined as the coefficient of resistance. On this basis, to describe swimming at low Reynolds (Re) numbers, two sets of

[a] *National Key Laboratory of Science and Technology for National Defence on Advanced Composites in Special Environments, Harbin Institute of Technology, Harbin 150001, P. R. China. E-mail: wangcg@hit.edu.cn*
[b] *Institute of Mechanical Engineering, Ecole Polytechnique Fédérale de Lausanne, CH-1015 Lausanne, Switzerland*
[c] *Department of Aeronautics and Astronautics, Fudan University, Shanghai 200433, P. R. China*
[d] *College of Sciences, Northeastern University, Shenyang 110819, P. R. China*

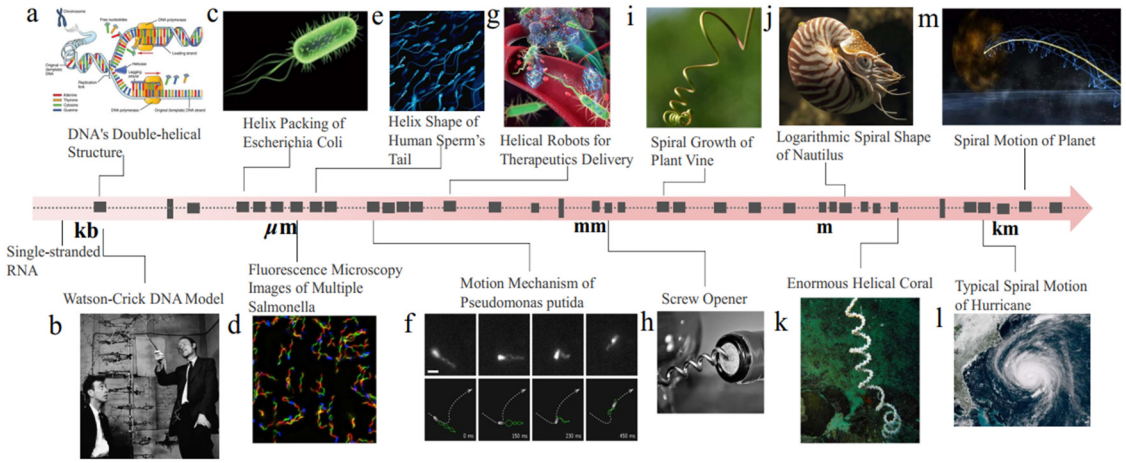

Fig. 1 Multifarious helical architectures or natural phenomena that follow spiral trajectories in different dimensions. (a) DNA replication process. The original DNA molecule is uncoiled by DNA helicase, separating the two strands. Each then forms the template upon which DNA polymerase synthesizes a new double-helical structure. (Figure courtesy of OpenStax College, The nucleus and DNA replication, https://www.cnx.org/content/m46073/1.4/). (b) The double helix model of DNA was proposed by J. D. Watson and P. H. C. Crick in 1953.[1] (c) The spiral flagella of *E. coli*. (d) The fluorescence microscopy images of *Salmonella* with multiple flagella.[2] (e) The swimming mode of the human sperm is rotating with the "head" as a center, and the spiral movement cleverly offsets the unilateral swing, to achieve symmetry. (f) A sequence of intermediate flagellar configurations that occur in the course of transition from a pulling to a wrapped bundle.[3] (g) Schematic diagram of the biomimetic mineralization of tumor-targeting *E. coli* for the delivery of therapeutics.[5] (h) Spiral-shaped wine opener. (i) Plants control their organs (such as stems, vines, leaves, *etc.*) under the action of auxin to produce spiral growth. (j) The inner walls of nautilus have visible spiral lines. The number of the lines is related to the lunar cycle around the Earth. (k) Large spiral coral up to 3 m long in the deep sea. (l) Weather map of a destructive helical hurricane hitting the coast (image from NOAAs *via* Getty Images). (m) The planets in the solar system move in spiral orbits.

drag coefficients[21] are introduced, assuming that the effect of each small segment is only locally important.

Previous studies show that a helix could be a class of structures that provides rich design options. Theoretical models have been established to analyze the force and torque of the helical structures;[22] however, they fail to predict when the geometrical parameter is close to zero, which means the helix degenerates to a cylinder or filament that produces zero thrust. In addition, when describing the motion performance of swimming *Escherichia coli*[23] and spirochetes,[24] such as super helices, there is a distinct divergence between the experimental results and theoretical solutions. Pioneers neglect hydrodynamic interactions between flows in the case of small pitch,[24,25] resulting in an inaccurate prediction. Furthermore, previous studies have been well developed in theory and experiment,[15,16,23] while there is a gap in numerical calculations and analysis of how the geometric configuration affects the motion.

This paper is outlined as follows. Section 2 proposes a novel concept of a hierarchical helical swimming robot and the methodology of the numerical calculations based on the resistive force theory (RFT). Section 3 presents the validation of the model compared with the analytical solutions, illustrating the underlying relationship between mechanical properties (normalized thrust, drag force, and propulsion efficiency) and dimensionless key geometric parameters and evaluates the motion performance of various hierarchical helix-based configurations. Finally, the main conclusions of this work are drawn in Section 4.

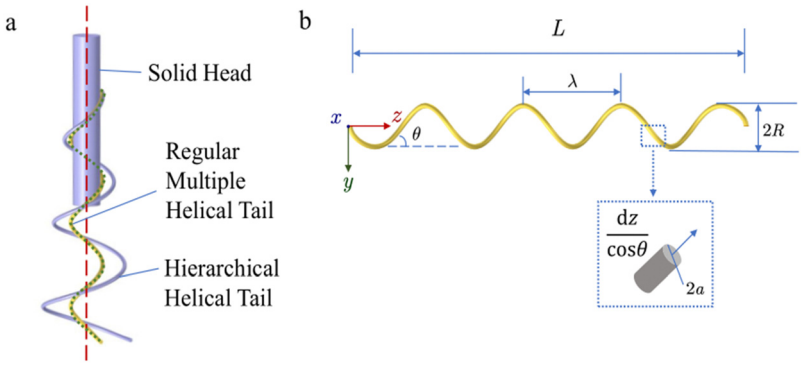

Fig. 2 Schematic of the helical configuration. (a) Schematic illustration of the helix-based swimmers (head with a regular multiple helical tail/hierarchical helical tail) taken as inspiration for this study. (b) The main geometric parameters are radius R, pitch λ, axial length L, filament radius a, and pitch angle θ, where $\theta = \tan^{-1}(2\pi R/\lambda)$. Inset shows a filament segment of length $d_S = d_z/\cos\theta$.

Design strategy and methodology

1. The concept of the hierarchical helical design

It is important to remark that locomotion represents the key challenge for the miniaturization of swimming robots when the dimension is scaled down to micro- and nanoscales. According to the famous ''scallop theorem'',[26] the swimming action of the conventional scallop shell structure cannot yield the desired propulsive effect since the inertial force is almost negligible in the face of viscosity in the microcosmic world. Some bacteria, such as *Escherichia coli*, and *Helicobacter pylori*, have already worked out their ways to sail in biological fluids. Inspired by these natural helical structures, pioneers[15,27,28] designed swimming machines driven by rotation of the spiral tail, like the screw of a bottle opener. Although the field is in its infancy, proof-of-concept examples have already demonstrated tremendous potential. Beyond the realization of ''getting around'', it becomes more challenging to enable them *in vivo* to accomplish tasks quickly, efficiently, and stably. For example, a swarm of bots can carry out targeted treatment or precision delivery to lesions with various speed levels to enable continuous supply. Inspired by the bacterial structure, we have designed the head and regular multiple helical tail/hierarchical helical tail (Fig. 2(a)). Fig. 2(b) shows the geometric parameters for theoretical analysis and numerical calculations.

2. Hydrodynamics analysis based on RFT

Propulsion mechanisms of micro-swimmers can be imitated as artificial propulsion systems to operate in low Re number environments. It is worthwhile to remark that, for a millimeter or centimeter swimmer, to ensure the equivalence of research results, we need to use a flow field with appropriate viscosity to ensure the premise of low Re regimes. Therefore, silicone oil is adopted here to replace biological fluids, such as blood. The Re number can be calculated by $\mathrm{Re} = \frac{VL\rho}{\mu}$, where V is the maximum characteristic fluid velocity, L is the characteristic length of the propeller, and ρ and μ are the density and the dynamic viscosity of the fluid, respectively. Herein, the Re number in the theoretical analysis and all subsequent simulation cases is 0.814 (lower than 1).

Stokes flow is a type of fluid flow where the advective inertial forces are much smaller compared with the viscous forces. The equations of motion for Stokes flow, called the Stokes equations (eqn (1)), are a linearization of the Navier–Stokes (N–S) equation (The detailed simplified derivation is provided in Appendix I), together with continuity conditions, given as follows:

$$\begin{aligned} \nabla\cdot\mathbf{V} &= 0 \\ -\nabla p + \mu\nabla^2\mathbf{V} &= 0 \end{aligned} \tag{1}$$

where $\mathbf{V}$ is the velocity vector, and ∇p is the pressure gradient. By neglecting the inertial terms, the simplified N–S equation achieves a linear and time-independent relationship between pressure forces and viscous forces, which is quite important to explain locomotion in low Re regimes. Consequently, the motion of the symmetrical helical swimmer,[29] with the total external force F and torque T can be described only by three constants, which is expressed in a matrix as follows:

$$\begin{bmatrix} F \\ T \end{bmatrix} = \begin{bmatrix} A & B \\ B^{\mathrm{T}} & C \end{bmatrix} \cdot \begin{bmatrix} U \\ \Omega \end{bmatrix} \tag{2}$$

where U is the linear velocity along the body axis, and Ω is the rotating angular velocity. The coefficients A, B, and C in the matrix depend on the fluid viscosity and otherwise on the geometrical parameters of the helical swimmer, which can be estimated as:[30]

$$\begin{aligned} A &= \left(\eta_{\parallel}\sin^2\theta + \eta_{\perp}\cos^2\theta\right)\frac{L}{\cos\theta} \\ B &= R\left(\eta_{\parallel} - \eta_{\perp}\right)L\sin\theta \\ C &= R^2\left(\eta_{\parallel}\cos^2\theta + \eta_{\perp}\sin^2\theta\right)\frac{L}{\cos\theta} \end{aligned} \tag{3}$$

where $\theta = \tan^{-1}\left(\frac{2\pi R}{\lambda}\right)$, and λ is the pitch of the helix. R is the radius of the helix. In eqn (3), $\eta_{\parallel}$ and $\eta_{\perp}$ are the commonly-used

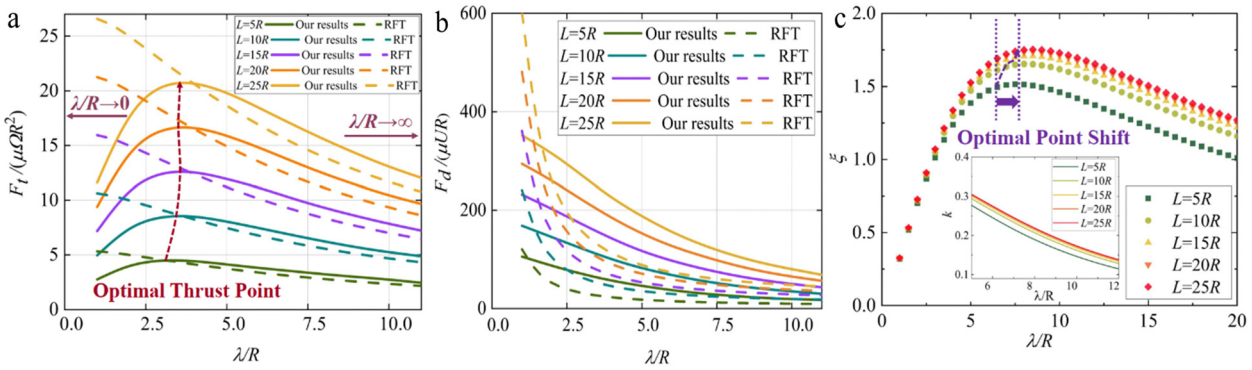

Fig. 3 The force and efficiency are influenced by the dimensionless geometric parameters. Normalized (a) thrust and (b) drag generated by the helix as a function of normalized λ concerning the radius R. The solid lines represent our numerical results, while the dashed lines are the analytical solutions of RFT. (c) Propulsion efficiency shows an optimal point shift as the body length increases. The inset presents the slope k of the propulsion efficiency near the optimal region, indicating the influence of characteristic length on the growth rate.

drag coefficients by Gray and Hancock,[21] respectively, being expressed as

$$\eta_{\perp} = \frac{2\pi\mu}{\ln\frac{2\lambda}{a} - \frac{1}{2}},\ \eta_{\parallel} = \frac{4\pi\mu}{\ln\frac{2\lambda}{a} + \frac{1}{2}} \tag{4}$$

where a is the radius of the filament. The geometric parameters mentioned above can be detailed as in Fig. 2(b).

For eqn (2)–(4), the item related to linear velocity U dominates the drag force F_d of the swimmer in a hydrodynamic environment, while rotating velocity Ω contributes to the thrust force F_t.

The propulsion efficiency can be indicated by a coefficient ξ,[15] as a symbol of the competition between drag and thrust, which can be expressed as

$$\xi = \frac{10000R\left(\eta_{\parallel} - \eta_{\perp}\right)L\sin\theta}{\left(\eta_{\parallel}\sin^2\theta + \eta_{\perp}\cos^2\theta\right)\frac{L}{\cos\theta} + 6\pi\mu a} \tag{5}$$

The detailed results of the force and efficiency will be reported in the next section. See Fig. 3.

3. Modeling methods

According to the above-mentioned low Re number environment, here the swimmers are established in two separated hydrodynamic cylindrical domains by the means of COMSOL Multiphysics®. The inside domain provides rotation implemented by a moving mesh, and the outside cylinder helps to emulate the axial propulsion of the swimmer by input/output flows. Frozen rotor approximation is performed in the simulation to increase the computing efficiency obviously. With this setting, the swimmer does not rotate during the calculation process; however, rotation and associated momentum terms are implanted in the flow. Therefore, a pseudo-steady-state condition of the helical rotation dynamics can reduce the execution time significantly. The force can be easily achieved through the integration of total stress along the rotating/longitudinal axes. The results will be indicated in the next section (see Appendix II).

Results and discussion

Results of normalized thrust and drag force of the helical structure in Fig. 2(b) are compared between classical RFT theoretical solutions and our works, as shown in Fig. 3(a and b). Our results are in good agreement in the monotonic declining region. However, it is important to remark that, for the small-size swimmers and even micro-size helix-based structures, for which λ/R is close to zero, there is a significant discrepancy between RFT and our results. In particular, the normalized drag forces in RFT increase exponentially as the pitch approaches zero, which is obviously not accurate. In conclusion, our results indicate that the numerical method *via* the Computational Fluid Dynamics (CFD) Module based on RFT is a good approach for analyzing the mechanical properties of swimmers at the microscopic scale and provides a supplement for conventional RFT. Fig. 3(c) illustrates the propulsion efficiency ξ for normalized λ concerning the radius R. The efficiency increases, then decreases with the normalized pitch. As can be observed, the long length shows a positive effect on the propulsion efficiency, while the optimal efficiency points occur shifted to the right as the length increases, which means that the number of turns probably dominates the propulsive efficiency. The increase of helix pitch gradually slows down the decreasing speed of propulsion efficiency; oppositely, the extension of the body length promotes the tendency to a depressed

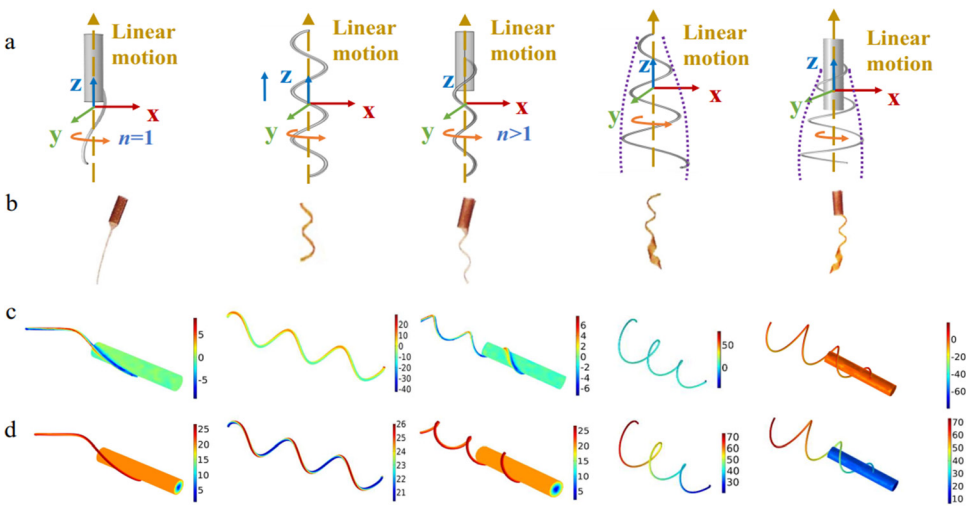

Fig. 4 Design and development of the bioinspired helix-based swimmers. The rotating frequency here used is 5 Hz. (a) Schematic diagram of the helix-based micro-swimming robots: from left to right, there are the head + planar tail (HPT) structure, only tail (OT) structure, head + multiple helical tail (HMT) structure, tail-shaped head + tail (TT) structure and head + hierarchical helical tail (HHT) structure. n is the number of turns of the helical tail. (b) The optical images of the helix-based swimmers, manufactured by a kirigami approach to building mass customized flexible micro-swimmers through single-step photolithography, corresponding to the schematic diagrams. Scale bars, 1 mm. (c) Cloud pictures of the pressure generated around different kinds of helix-based structures. Unit: Pa. (d) Forward velocity cloud comparisons. Unit: mm s^{-1}.

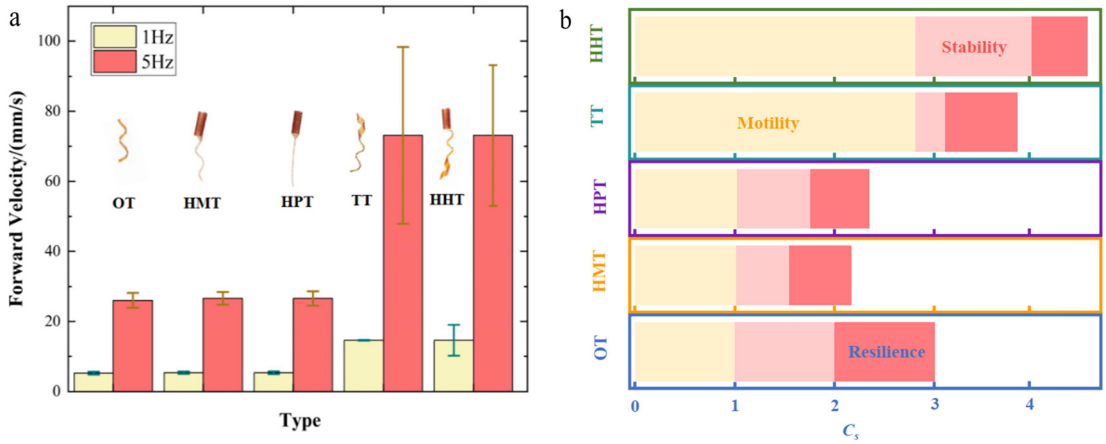

Fig. 5 Comparison of comprehensive athletic ability and optimization of maneuverability. (a) Quantitative comparison of forwarding velocity for different prototypes. The swimmers are driven at 1 Hz/5 Hz, respectively. (b) A general diagram evaluates the comprehensive motion performance of different helix-based structures from three indicators: motility, resilience, and stability. Based on the motion behavior of OT, the performance of the other four structures is explained by the dimensionless parameter C_s.

efficiency (Fig. 3(c)). As for the hierarchical helical tail in Fig. 2(a), Koens *et al.*[31] carried out the parametric sweeps for its influence on the motion performance of the structure, while it is not the research focus of this work.

Previous work has shown that for sizes close to or even lower than a micron, such as bacterium, and sperm, our method is a reliable and a time-saving approach to estimate the swimming performance of the helical robots. Here, we systematically explore the potential advantage of this morphological diversity by building helix-based swimmers with different body structures (Fig. 4(a and b)). The forward velocity and pressure generated around the swimmers are reported to provide a more accurate comparison of performance (Fig. 4(c and d)). The structures with hierarchical tails reveal an impressive advantage in velocity.

Here the forward velocities of different kinds of helix-based structures are reported to provide a more precise comparison of the performance. The forward velocity grows linearly with the increase of the rotational frequency of these five different kinds of helix-based structures (Fig. 5(a)). With the addition of the head, there is a slight 2.2% increase in velocity compared with the foundational only tail (OT) swimmer who has only a helical tail. However, for the tail-shaped head + tail (TT) structure with an exponential envelope and radial pitch, the forward velocity has made a qualitative leap, rising by 180.3%. Nevertheless, the standard deviation has markedly increased because of the increase in rotational angular velocity, which means that the improvement is not very stable. The presence of more turns is advantageous as the helix can generate torque and propulsion, which can be observed from the comparison between the head + multiple helical tail (HMT) structure and the head + planar tail (HPT) structure. The head + hierarchical helical tail (HHT) structure and the TT structure show almost identical velocity growth, while HHT is less stable at a low rotation frequency and exhibits advantages at a higher rotation frequency.

The swimming performance of the various kinds of helix-based robots is observable in Fig. 5(b), in which comprehensive evaluation is carried out through three indicators: motility, resilience, and stability. To make the comparison open-and-shut, the dimensionless parameter C_s is adopted here and the three indexes of OT structure are taken as the basis of comparison to give a unified standard of several structures studied in this work. From this perspective, we express C_s as C_{other}/C_{OT}, where C_{other} represents the performance displayed by the head + multiple helical tail (HMT) structure, the head + planar tail (HPT) structure, the tail-shaped head + tail (TT) structure, or the head + hierarchical helical tail (HHT) structure, while C_{OT} denotes the property shown by the OT structure. Here, we express motility as $U/fL \times 1000$,[16] where U is the linear velocity, f is the rotating frequency, and L is the body length. Through the available experimental data from Fazil *et al.*,[16] a quantitative comparison of reorientation times for different prototypes could be obtained and we deal with the recovery time by $\frac{\log(1000 \times t_{OT}/t_{other})}{3}$, where t_{OT} and t_{other} represent the time during the reorientation of the swimming direction of the OT structure and the other structure, respectively. By calculating the average pressure generated around the body, we provide an assessment of the stability. OT and TT structures show the best performance in resilience as expected because they do not deal with body and tail coordination and have high structural symmetry. If the motility is the core metric, TT and HHT structures appear to be the clear choices over several other structural designs. To integrate a cluster system as stable as possible, the HHT or OT structures or their combinations are worth considering.

Furthermore, for some specific applications, such as the swarming micro- or nano-robots for medical purposes, some of them play the role of the pioneer to rapidly reach the area which needs emergency surgery, while the others take the responsibility of postoperative rehabilitation by drug delivery and release. Therefore, our diagram (Fig. 6) aims at providing a guideline to choose hierarchical helix-based structures with different forward velocities. EH, RH, and SH represent the

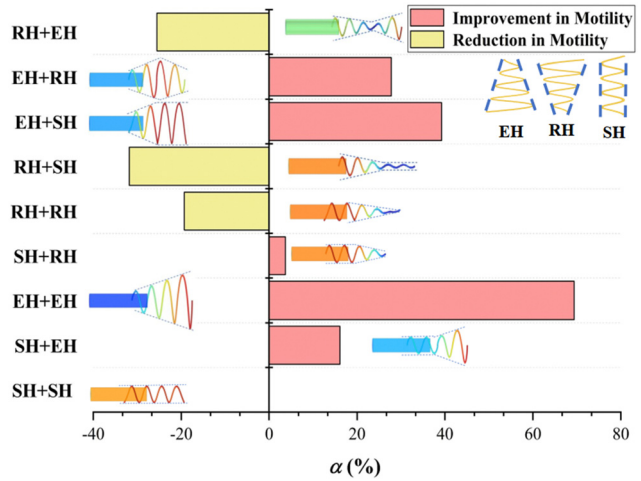

Fig. 6 The hierarchical helical design with variable configurations and the relative variance ratios of motility compared with the SH + SH structure. All the swimmers share the same head size, rotating in the same viscosity flow field of 96.4 mPa·s at 5 Hz. EH, RH, and SH represent the emanative hierarchical structure, retractile hierarchical structure and straight structure, respectively. Each column in the bar chart corresponds to the results of the different structures based on the combinations of these three configurations.

emanative hierarchical structure, retractile hierarchical structure and straight structure, respectively. α is the relative variance rate in the motility of all the swimmers compared with the SH + SH structure. Here, we conduct a combination of multiple kinds of hierarchical helical tails. The EH + EH structure shows outstanding performance in motility so there is an outstanding 69.4% improvement on the basis of the SH + SH structure. This is due to the fact that the trumpet-shaped EH structure concentrates larger thrust force and torque at the far-end to drive motion, allowing rotation to dominate. However, with the intervention of the RH structure that is like a funnel, the improvement effect on the motility is remarkably weakened and even reversely reduced, such as the SH + RH, RH + RH, and RH + SH structures. By comparing EH + EH, EH + SH, EH + RH, and RH + EH, it is not difficult to find that the hierarchical helical swimmer is more susceptible to the front-end configuration. In other words, the configuration closer to the head governs the tendency of velocity growth or deceleration. The contribution of the RH structure to deceleration can be readily explained by the extreme case that the hierarchical helix is infinitely stretched (the radial radius approaches zero) and the end of the tail becomes a straight filament that manifests itself as a loss of motility. As stable as possible, the HHT, OT structures or their combinations are worth considering.

Conclusions

In summary, this paper introduces a type of hierarchical helical swimmer, which combines mechanical attributes of remarkable motility along with relatively high stability and resilience. A numerical model is developed to investigate the relationship between the key mechanical indicators (thrust force, drag force and propulsion efficiency) with the dimensionless geometric parameters, which agrees well with resistive force theory. A significant increase by nearly twice demonstrates that the hierarchical helical structures can offer higher propulsion than various existing typical helical structures. The combination design based on multiple different hierarchical helical configurations is shown as a reliable strategy to obtain the velocity controllability (68.2–169.4%) of practical interest. The front–end structure plays a dominant role in affecting the motion performance. Collectively, the combined study of mechanics modeling, numerical calculations and available experimental measurement presented herein provides systematic guidelines for the application and manufacture of functional swimming micro-robots.

Author contributions

Z. Y. Zhang developed the conceptualization and methodology of the work. The original draft was written by Z. Y. Zhang and then edited in detail by Y. F. Wang and reviewed by all the authors. J. T. Kang provided the inspiration for this work. The investigations and simulations were performed by Z. Y. Zhang with the assistance of X. H. Qiu. The project was supervised by C. G. Wang who also acquired the funding and administered the project.

Conflicts of interest

There are no conflicts to declare.

Appendix

I The simplification of the Navier–Stokes equations in a low Reynolds regime

Flow field for a Newtonian fluid is described by Navier–Stokes and continuity equations given as follows:

$$\begin{aligned} \nabla.\mathbf{V} &= 0 \\ \rho\frac{\mathrm{D}\mathbf{V}}{\mathrm{D}t} &= -\nabla p + \mu\nabla^2\mathbf{V} + \rho\mathbf{g} \end{aligned} \tag{A1}$$

where $\mathbf{V}$ is the velocity vector, ∇ is the nabla operator, ρ and μ are the density and the dynamic viscosity of the fluid, t is the time, and $\frac{\mathrm{D}}{\mathrm{D}t}$ represents total derivative. In this equation, $\frac{\mathrm{D}\mathbf{V}}{\mathrm{D}t} = \frac{\partial\mathbf{V}}{\partial t} + (\mathbf{V}\cdot\nabla\mathbf{V})$, ∇p is the pressure gradient and $\rho\mathbf{g}$ denotes the gravity. Figuratively speaking, the second equation of eqn (A1) is the expression of Newton's second law applied to the fluid, in which $\rho\frac{\mathrm{D}\mathbf{V}}{\mathrm{D}t}$ represents the acceleration per unit volume. The equation can be simplified to Stokes equations if we are interested in low Reynolds number flow, which is known

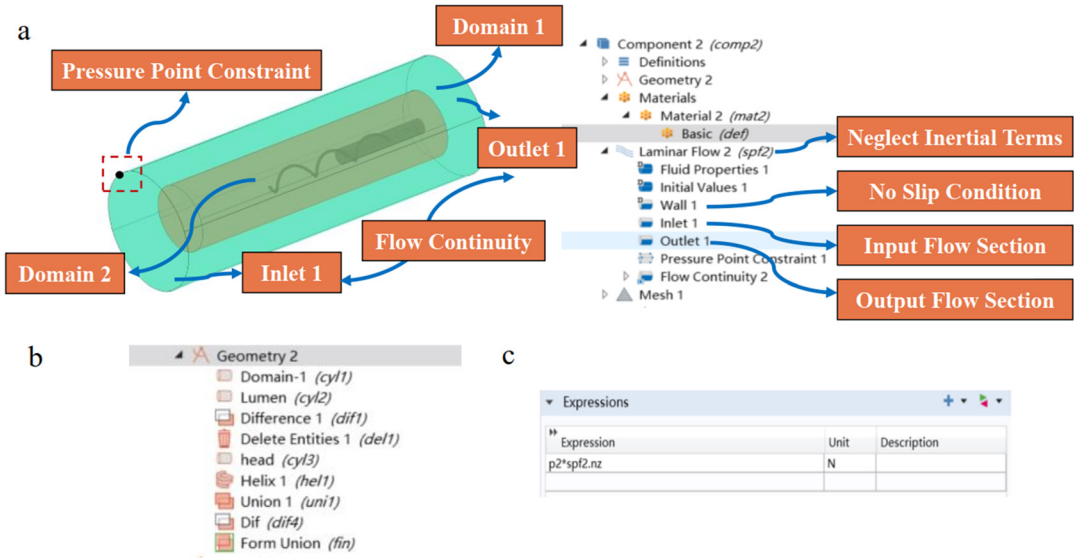

Fig. 7 The modeling details in COMSOL Multiphysics®. (a) The model of the helical swimming structure within a lumen flow environment and the laminar flow drop-down menu. (b) The process of the geometry building up. (c) The expression inserted for the surface integration to obtain the thrust or drag force.

as Stokes flow in general. Stokes flow is a type of fluid flow where the advective inertial forces are much smaller compared with the viscous forces. In detail, $\frac{\partial \mathbf{V}}{\partial t}$ is zero for the steady-state flow and $\mathbf{V}.\nabla\mathbf{V}$ is the inertial term that can be neglected in terms of the Stokes flow. The gravity can also be neglected here.

Therefore, we can obtain the simplified expression of the N–S equations as follows:

$$\nabla\cdot\mathbf{V} = 0$$
$$-\nabla p + \mu\nabla^2\mathbf{V} = 0 \qquad \text{(A2)}$$

in which a linear relationship between pressure forces and viscous forces is achieved. In Stokes equations we can see the time reversible property of the fluid flow, which is quite important to explain locomotion in low Reynolds regimes.

II The numerical modeling details

The modeling schematic is shown in Fig. A1(a). Based on RFT, a low Re regime implies that the linear and rotational velocity contributions are additive. Consequently, the numerical modeling can be divided into two independent domains: the external domain to emulate longitudinal motion and the inner one to perform rotation. This distinction significantly simplifies the complexity of the helix motion. The head + multiple helical tail (HMT) structure is established inside the inner rotating domain. For the geometry of the helical structure (as shown in Fig. A1(b)): (1) we build up the head (a cylinder) and the tail (a helix) in the appropriate spatial position and use the union selection to combine these two parts. (2) The difference selection is used to distinguish the helical swimmer and the fluid environment. (3) Finally, we choose form union to make all the geometry as a whole. For the materials setting, the lumen is filled with silicon oil to ensure that a low Re condition is achieved. The material parameters are set as in Table A1. For the mesh, due to the combination of the head and helical tail, the corner refinement needs to be carried out.

A laminar flow is implemented by means of the Computational Fluid Dynamics (CFD) Module for each part, as shown in Fig. A1(a). Thus, it is possible to emulate a Stokes flow in which inertial terms are rejected. In addition, a no-slip condition is attached to the surface of the helix and the lumen, which ensures that the fluid will have zero velocity relative to these boundaries. The longitudinal motion of the swimmer is achieved by including an input/output flow into the lumen. Here we use the fully developed flow with a flow rate 6×10^{-4} m^3 s^{-1}. To perform rotation on the inner domain, it is necessary to add the moving mesh on the cylindrical domain 2 (Fig. A1(a)). In this case, a rotating angular velocity Ω moving mesh is implemented and attached to the inner cylinder. Here we set the angular velocity as 6.283 rad s^{-1} and 31.416 rad s^{-1}, respectively (corresponding to 1 Hz and 5 Hz in the results shown in Fig. 5(a)). A frozen rotor approximation is included in the numerical calculation to significantly reduce the execution time. In other words, the helical structure inside does not rotate during the execution; however, rotation and associated momentum terms are imparted to the flow. Therefore, it is possible to obtain a pseudo-steady-state condition of the helical rotation dynamics.

To investigate the effect of the geometrical parameters of the helical structure on the swimming performance

Table 1 Fluid parameters used in the numerical modeling

Property	Value	Unit
Fluid density	964	kg m^{-3}
Fluid viscosity	0.0964	Pa s
Angular velocity	6.283/31.416	rad s^{-1}
Linear flow rate	6×10^{-4}	m^3 s^{-1}

(the results shown in Fig. 3), the parametric sweep in this study is considered here for the helix pitch λ and axial length L. The normalized pitch varies from R to $20R$ with a step of $R/2$. Likewise, five different values of the helix tail's lengths L are calculated ($5R$, $10R$, $15R$, $20R$, and $25R$). For the output and post-processing of the results: (1) it is very easy to obtain the cloud pictures and derived values of the velocity and pressure by creating the 3D-plot group. Here we show the results in terms of surface. (2) To get the thrust force and the drag force, surface integration is performed to obtain the simulation results using the expression in Fig. A1(c) (the propulsive and rotation motion are along the z axis). For eqn (2)–(4), the item related to linear velocity U dominates the drag force F_d of the swimmer in a hydrodynamic environment, while rotating velocity Ω contributes to the thrust force F_t. Therefore, when the helix rotates at the speed of Ω, thrust force is estimated computing the integration of total stress parallel to the helix (z axis). In the same way, it also allows us to estimate drag force when the helix moves at a linear speed U. (3) Simulated results mentioned above are compared with RFT results through MATLAB and Origin.

III Materials and experimental platform

Silicon oil is used to simulate a Stokes flow in the lumen, with the density of 964 kg m^{-3} and viscosity of 0.0964 Pa s^{-1}, respectively. Due to the adoption of the frozen rotor study, the helical swimmer can be treated as a frozen part without material deformation.

The available experimental data of the discussion on the resilience of the swimmers are from Fazil *et al.*[16] *N*-Isopropylacrylamide (NIPAAm) as the monomer, acrylamide (AAm) as the hydrophilic comonomer, 2,2-dimethoxy-2-phenylacetophenone (99%) as the photoinitiator, and poly (ethylene glycol) diacrylate (PEGDA; average molecular weight, 575) as the cross-linker are all purchased from Sigma-Aldrich.

The engineering of magnetically controlled micro-machines is independently programmed by incorporating magnetic nanoparticles (MNPs) into sequentially patterned hydrogel layers. The magnetic actuation principle is used to reproduce the motions of natural swimming microorganisms with helical flagella. Ultraviolet lamps (Lightning Enterprises, USA) were integrated inside the solenoid to initiate the cross-linking of the hydrogel polymers. The maximum strength of generated uniform magnetic fields by the solenoid and Helmholtz coils are 10 and 5 mT at the center region, respectively. The motion studies were conducted with a custom design eight-coil electromagnetic manipulation system that is called OctoMag.[32]

Acknowledgements

This work is supported by the National Natural Science Foundation of China 12172102 and China Scholarship Council. Z. Y. Zhang gratefully acknowledges Prof. Selman Sakar for his comments and advice. The authors thank A. Dolev and Y. C. Zhang for their suggestions on simulations and F. E Uslu's assistance with the experiments. The authors wish to thank Mr W. Zhang, Mrs X. M. Tang, and Mr Y. F. Shen for their thoughtful kindness. The authors would like to express their thanks to the editor and anonymous reviewers whose constructive comments significantly improved this letter.

References

1 J. D. Watson and F. H. Crick, *Nature*, 1953, **171**, 737–738.
2 K. T. Hughes, *Curr. Biol.*, 2017, **27**, R413–R415.
3 M. Hintsche, V. Waljor, R. Grossmann, M. J. Kuhn, K. M. Thormann, F. Peruani and C. Beta, *Sci. Rep.*, 2017, **7**, 16771.
4 Q. Yang, X. Wan, J. Wang, Y. Zhang, J. Zhang, T. Wang, C. Yang and Z. Ye, *Hortic. Res.*, 2020, **7**, 180.
5 S. Yan, X. Zeng, Y. Wang and B. F. Liu, *Adv. Healthcare Mater.*, 2020, **9**, e2000046.
6 J. Li, B. E.-F. de Ávila, W. Gao, L. Zhang and J. Wang, *Sci. Rob.*, 2017, **2**, eaam6431.
7 W. Hu, G. Z. Lum, M. Mastrangeli and M. Sitti, *Nature*, 2018, **554**, 81–85.
8 J. Zhu, M. Dexheimer and H. Cheng, *npj Flexible Electron.*, 2017, **1**, 1–13.
9 M. Liu, T. Zentgraf, Y. Liu, G. Bartal and X. Zhang, *Nat. Nanotechnol.*, 2010, **5**, 570–573.
10 P.-S. Huang, G. Oberdorfer, C. Xu, X. Y. Pei, B. L. Nannenga, J. M. Rogers, F. DiMaio, T. Gonen, B. Luisi and D. Baker, *Science*, 2014, **346**, 481–485.
11 X. Cheng and Y. Zhang, *Extreme Mech. Lett.*, 2021, **42**, 101114.
12 H. Alemzadeh, J. Raman, N. Leveson, Z. Kalbarczyk and R. K. Iyer, *PLoS One*, 2016, **11**, e0151470.
13 F. Nadal and E. Lauga, *Phys. Fluids*, 2014, **26**, 082001.
14 J. L. Moran and J. D. Posner, *Annu. Rev. Fluid Mech.*, 2017, **49**, 511–540.
15 G. H. Tiantian Xu, N. Andreff and S. Régnier, *J. Microbio Robot.*, 2016, **11**, 57–66.
16 H.-W. Huang, F. E. Uslu, P. Katsamba, E. Lauga, M. S. Sakar and B. J. Nelson, *Sci. Adv.*, 2019, **5**, eaau1532.
17 B. Dai, J. Wang, Z. Xiong, X. Zhan, W. Dai, C. C. Li, S. P. Feng and J. Tang, *Nat. Nanotechnol.*, 2016, **11**, 1087–1092.
18 D. Fan, Z. Yin, R. Cheong, F. Q. Zhu, R. C. Cammarata, C. L. Chien and A. Levchenko, *Nat. Nanotechnol.*, 2010, **5**, 545–551.
19 G. I. Taylor, *Proc. R. Soc. London, Ser. A*, 1952, **214**, 158–183.
20 J. Lighthill, *SIAM Rev.*, 1976, **18**, 161–230.
21 J. Gray and G. Hancock, *J. Exp. Biol.*, 1955, **32**, 802–814.
22 B. Rodenborn, C. H. Chen, H. L. Swinney, B. Liu and H. P. Zhang, *Proc. Natl. Acad. Sci. U. S. A.*, 2013, **110**, E338–347.
23 S. Chattopadhyay and X. L. Wu, *Biophys. J.*, 2009, **96**, 2023–2028.

24 J. Yang, C. W. Wolgemuth and G. Huber, *Phys. Rev. Lett.*, 2009, **102**, 218102.
25 A. Ghosh and P. Fischer, *Nano Lett.*, 2009, **9**, 2243–2245.
26 E. M. Purcell, *Am. J. Phys.*, 1977, **45**, 3–11.
27 M. Kong, Y. Wu, G. Li and R. G. Larson, *Soft Matter*, 2015, **11**, 1572–1581.
28 W. Huang and M. Jawed, *Soft Matter*, 2020, **16**, 604–613.
29 E. M. Purcell, *Proc. Natl. Acad. Sci. U. S. A.*, 1997, **94**, 11307–11311.
30 J. J. Abbott, K. E. Peyer, M. C. Lagomarsino, L. Zhang, L. Dong, I. K. Kaliakatsos and B. J. Nelson, *Int. J. Robot. Res.*, 2009, **28**, 1434–1447.
31 L. Koens, H. Zhang, M. Moeller, A. Mourran and E. Lauga, *Eur. Phys. J. E: Soft Matter Biol. Phys.*, 2018, **41**, 1–14.
32 M. P. Kummer, J. J. Abbott, B. E. Kratochvil, R. Borer, A. Sengul and B. J. Nelson, *IEEE Trans. Robot.*, 2010, **26**, 1006–1017.